Electrolytic fluid speciation by Gibbs energy minimization and implications for subduction zone mass transfer

James A.D. Connolly *, Matthieu E. Galvez

Department of Earth Sciences, Swiss Federal Institute of Technology, CH-8092 Zurich, Switzerland

A B S T R A C T

The number of solute species required to describe the thermodynamic behavior of electrolytic fluids is a hindrance to the incorporation of aqueous geochemistry in petrological Gibbs energy minimization procedures. An algorithm is developed to overcome this problem. Beginning from the solute-free limit, chemical potentials, and phase stability are determined by minimization, the solute speciation and bulk fluid properties consistent with these chemical potentials are then computed and the procedure repeated until the chemical potentials converge. Application of the algorithm to a model for metamorphism of subducted sediment shows that accounting for solute chemistry does not change the conclusion based on molecular fluid models that a pervasive water flux from the subjacent mantle is required to explain island-arc carbon emissions by fluid-mediated slab decarbonation. This putative flux would deplete the sediment in potassium, limiting the capacity of the slab to transport water to greater depth and rendering it refractory to melting.

© 2018 Elsevier B.V. All rights reserved.

1. Introduction

Gibbs energy minimization is applied to a broad spectrum of geochemical and petrological problems (Leal et al., 2017). In geochemistry the focus of these applications is usually reactive transport (Wolery, 1992; Bethke, 1996), whereas in petrology the focus is predicting phase stability (DeCapitani and Brown, 1987; Connolly, 2009). This disparity has led to a situation in which many geochemical codes account for complex fluid chemistry, but seek only a local equilibrium solution, whereas petrologic codes seek a costly global solution that limits their ability to treat the complex fluid chemistry. As a means of bridging this gap Galvez et al. (2015, 2016) use phase equilibria computed by Gibbs energy minimization assuming a solute-free fluid to back-calculate solute chemistry. This method accurately estimates solute chemistry provided the solute mass is small compared to the total mass of the system, but is not well suited for reactive transport problems because the phase proportions and bulk fluid chemistry are not rigorously determined. The present work improves on this method by incorporating back-calculated fluid chemistry in an iterative Gibbs energy minimization procedure referred to here as lagged speciation. It should be remarked that

there are completely robust geochemical codes (Harvie et al., 1987; Karpov et al., 2001), which, at least in principle, are capable of treating petrological models.

The utility of the lagged speciation algorithm is demonstrated by a model for devolatilization of subduction zone sediments. This problem has been made tractable by the Deep Earth Water (DEW) model for electrolytic fluids (Sverjensky et al., 2014), which extends the Helgeson–Kirkham–Flowers (HKF) formulation (Shock et al., 1992) for aqueous species to high pressure conditions. Although a number of studies have considered the implications of the DEW model for fluid-dominated subduction zone chemistry (Facq et al., 2014; Sverjensky and Huang, 2015; Tumiati et al., 2017), the present focus is the rock-dominated limit appropriate in systems where the fluid is generated by devolatilization. This limit was investigated by Galvez et al. (2015) using a variant of the DEW model. The distinction between the DEW model and the Galvez et al. (2015) variant, is that in the DEW model the solvent is H_2O and molecular volatiles are treated as solute species, whereas in Galvez et al. (2015) the solvent is a mixture of molecular volatiles. Both approaches are compared.

Subduction zone devolatilization is topical because of its potential role in various global element cycles. The observation, based on simple sub-solidus phase equilibrium models (Kerrick and Connolly, 2001a, 2001b) that carbonates persist within subducted slabs beyond sub-arc depth has motivated alternative hypotheses to explain extensive slab decarbonation. These hypotheses include:

* Corresponding author.
  E-mail address: james.connolly@erdw.ethz.ch (J.A.D. Connolly).

infiltration-driven decarbonation (Connolly, 2005; Gorman et al., 2006); C transfer by entrainment or diapirism (Dasgupta et al., 2004; Behn et al., 2011); slab-melting (Poli, 2015; Skora et al., 2015); or near-surface provenance of volcanic CO_2 (Mason et al., 2017). With the exception of the latter, all of these mechanisms are viable but unsatisfying in that they require a coincidence of processes or extreme temperatures. Evidence of sub-solidus carbonate dissolution (Frezzotti et al., 2011; Ague and Nicolescu, 2014) has prompted the suggestion that, by neglecting the solubility of non-volatile elements, early models underestimated the efficacy of simple decarbonation processes. Previous work (Kelemen and Manning, 2015) indicates dissolution may cause a two-fold increase in the carbon-content of subduction zone fluids, but does not address fluid production. The models here extend that work by tracking fluid evolution from the surface to beyond sub-arc depths.

This paper begins with a generalization of the back-calculation method (Galvez et al., 2015). The lagged speciation algorithm by which back-calculated results may be integrated into a Gibbs energy minimization procedure is then outlined and the limitations of the algorithm are explained. The final major section uses the subduction zone model to illustrate some technicalities of the method and to explore the consequences of solute chemistry on closed, open, and infiltration-driven devolatilization scenarios.

2. Back-calculated speciation

The term back-calculated speciation designates the calculation of the solute speciation of an electrolytic fluid under the assumptions of charge balance, equilibrium, known solvent composition, and specified chemical potentials (Galvez et al., 2015). The method follows by observing that the partial molar Gibbs energy of any species can be expressed

$$g^i = -n_{e-}^i \mu_{e-} + \sum_{j=1}^{c} n_j^i \mu_j \tag{1}$$

where c is the number of components, μ_j and μ_{e-} are, respectively, the chemical potential of component j and the electron, and for species i: n_j^i is the molar amount of component j, and $-n_{e-}^i$ is the molar charge, abbreviated hereafter q^i. Eq. (1) can be rearranged to express μ_{e-} in terms of the chemical potentials and the properties of charged species i

$$\mu_{e-} = \frac{1}{q^i}\left(g^i - \sum_{j=1}^{c} n_j^i \mu_j\right). \tag{2}$$

Because μ_{e-} is the same for all species at equilibrium, the partial molar Gibbs energy of any arbitrarily chosen charged species (g^i) can be related to the partial molar Gibbs energy of a charged reference species (g^k) by equating the right-hand-side of Eq. (2) for both species

$$\frac{1}{q^i}\left(g^i - \sum_{j=1}^{c} n_j^i \mu_j\right) = \frac{1}{q^k}\left(g^k - \sum_{j=1}^{c} n_j^k \mu_j\right). \tag{3}$$

Rearranging Eq. (3), the partial molar Gibbs energies of any charged species can then be expressed in terms of the reference species partial molar Gibbs energy and the chemical potentials of the system

$$g^i = \frac{q^i}{q^k}\left(g^k + \sum_{j=1}^{c} \mu_j \Delta n_j^i\right) \tag{4}$$

where $\Delta n_j^i = n_j^k - n_j^i$. In terms of a solute reference state activity model, the partial molar Gibbs energies in Eq. (4) are

$$g^i = g^{*,i} + RT \ln\left(m^i \gamma^i\right) \tag{5}$$

where $g^{*,i}$ is the solute reference state molar Gibbs energy, m^i is the molal concentration, γ^i is the activity coefficient, T is absolute temperature, and R is the universal gas constant. Applying Eq. (5) in Eq. (4) and rearranging the result

$$m^i = \frac{c^i}{\gamma^i}\left(m^k \gamma^k\right)^{q^i/q^k} \tag{6}$$

where

$$c^i = \exp\left(\frac{1}{RT}\left\{\frac{q^i}{q^k}\left[g^{*,k} + \sum_{j=1}^{c} \mu_j \Delta n_j^i\right] - g^{*,i}\right\}\right).$$

Substituting Eq. (6) into the charge balance constraint for a fluid with s charged solute species

$$\sum_{i=1}^{s} q^i m^i = 0 \tag{7}$$

yields

$$\sum_{i=1}^{s} \frac{q^i c^i}{\gamma^i}\left(m^k \gamma^k\right)^{q^i/q^k} = 0, \tag{8}$$

which can be solved in the ideal limit ($\gamma^i \rightarrow 1$) for m^k if the composition of the solvent, which influences $g^{*,i}$, is known. The concentrations of the remaining charged species are then obtained from Eq. (6) and those of neutral species from Eq. (5).

In the non-ideal case, additional assumptions are necessary to compute the activity coefficients in Eqs. (5), (6), and (8). Regardless of those assumptions, the method is flawed: if the solvent composition is consistent with the specified chemical potentials, as is the case when the chemical potentials and solvent composition are obtained by Gibbs energy minimization, then finite solute concentrations violate this consistency. This flaw has the consequence that, except in the limit of infinite dilution ($m^i \rightarrow 0$), there is no bulk fluid composition that simultaneously satisfies Eq. (8) and the constraint on the chemical potentials of the system, i.e., there is no thermodynamically robust relation between fluid speciation and bulk composition.

3. The lagged speciation algorithm

The limitation of simple back-calculated speciation is the absence of a relation between the calculated solute chemistry and the bulk chemistry of the fluid, which precludes evaluation of mass balance constraints. To circumvent this limitation, the present work exploits the iterative aspect of Gibbs energy minimization by successive linear programming (Connolly, 2009). The essential feature of successive linear programming is that an initial result in which the compositions of the phases are discretized at some specified resolution is iteratively refined until a desired target resolution has been achieved. The innovation here is to use a minor modification of the back-calculated speciation algorithm to estimate the Gibbs energy and composition of the stable fluid(s). In the initial optimization, the fluid may contain multiple solvent species (e.g., H_2O, CO_2, CH_4, H_2S), but is solute-free. Given the solute-free solvent composition(s) and chemical potentials obtained in this optimization, the reference state solute partial molar Gibbs energies are computed, Eq. (8) is solved for the concentration of the reference ion, and Eqs. (5) and (6) are solved for the concentrations of the remaining solute species. The solvent mole fractions are then recomputed as
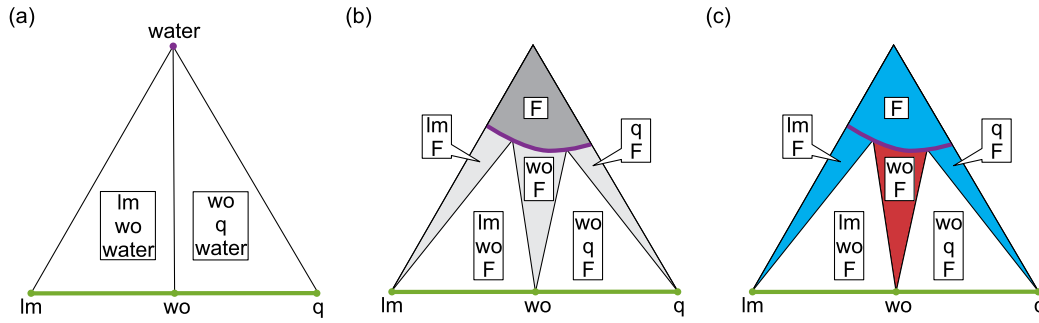
Fig. 1. Schematic phase relations for the H_2O–CaO–SiO_2 system at a condition such that fluid and stoichiometric wollastonite, lime, and quartz are the stable phases (see Table 1 for phase notation; H_2O is taken to be the sole component of the solvent). The fluid saturation (green) surface bounds bulk compositions at which no fluid is stable and is coincident with the CaO–SiO_2 join; the solid saturation surface (magenta) bounds bulk compositions at which no solid is stable. In the solute-free system (a), for any general composition, the stable phase assemblage is either lm + wo + water or wo + q + water. In the solute-bearing system (b), finite fields must exist for F, F + lm, F + q, and F + wo (gray-scale shading indicates phase field variance). Lagged speciation is infeasible for bulk compositions that lie within these high variance phase fields. In (c), the infeasible compositions are indicated in blue if infeasibility can be established from the necessary condition that the solids of the phase field contain all the non-solvent components of the system and in red if infeasibility can only be established by the more general sufficient condition discussed in the text. (Refer to the web version of this article for colored figures.)

$$y_{h+1}^i = \frac{m_h^i}{m_{total}} \quad i = t+1, \ldots, t+r \tag{9}$$

with

$$m_{total} = \sum_{i=1}^{t} m_h^i + \sum_{i=t+1}^{t+r} y_h^i \tag{10}$$

where t is the total (charged + neutral) number of solute species, r is the number of solvent species, and h indexes the iteration level. The specific Gibbs energy and bulk composition for the fluid used in the succeeding iteration are

$$g_{h+1} = \sum_{i=1}^{t} \left(m_h^i \left[g_{h+1}^{*,i} + RT \ln\left(m_h^i \gamma_h^i \right) \right] \right)$$

$$+ \sum_{i=t+1}^{t+r} \left(m_h^i \left[g^{0,i} + RT \ln\left(y_{h+1}^i \gamma_{0,h}^i \right) \right] \right) \tag{11}$$

$$n_{j,h+1} = \sum_{i=1}^{t} m_h^i n_j^i + \sum_{i=t+1}^{t+r} m_{h+1}^i n_j^i \quad j = 1, \ldots, c, \tag{12}$$

where $\gamma_{0,h}^i$ is the activity coefficient of solvent species i in the solute-free solvent. Eq. (11) ignores the dependence of the solvent species activity coefficients on solute concentration and is therefore thermodynamically consistent only in the ideal limit (e.g., Wolery, 1992). Although it is not algorithmically required, the inconsistent form is maintained because electrolytic fluid species activity models are currently poorly constrained. In contrast, molecular fluid equations of state are capable of predicting species activities in the solute-free solvent with good accuracy (Prausnitz, 1969). Excepting this inconsistency, and in contrast to simple back-calculation, iterative application of Eqs. (11) and (12) reaches a thermodynamically consistent solution provided the lagged chemical potentials, used to compute the solute molalities m_h^i by back-calculation, converge.

To distinguish back-calculation during lagged speciation from simple back-calculation (Galvez et al., 2015), simple back-calculation is defined as the solute species concentrations and fluid bulk compositions m_0^i and $n_{j,1}$, respectively, in Eq. (12).

3.1. Algorithmic limitations

The chemical potentials of all soluble components of a system are necessary to back-calculate fluid speciation. It follows that a necessary condition for lagged speciation is that any component

represented in the fluid only by solute species must be present in at least one phase other than the fluid. The nature of this limitation is illustrated schematically (Fig. 1) for the CaO–SiO_2–H_2O system under conditions such that stoichiometric lime (lm; see Table 1 for phase notation), wollastonite (wo), and quartz (q) are stable solids and the solvent is considered to consist only of H_2O. In simple back-calculation, the chemical potentials of all components are computed for the solute-free system (Fig. 1a). Thus, for any general bulk composition, the chemical potentials correspond to those of the assemblage lm + wo + water or wo + q + water. Each of these assemblages yields a fluid (F) composition that may be iteratively refined by lagged speciation to yield a point on the fluid-saturation surface of the system. In the course of this refinement, the lm + wo + F and wo + q + F phase fields shrink creating phase fields with finite area for lm + F, q + F, and F (Fig. 1b). The soluble components SiO_2 and CaO are not present in, respectively, lm and q. Therefore, the lagged speciation algorithm becomes infeasible during iteration for bulk compositions that lie within the lm + F, q + F, and F phase fields. A consequence of this limitation is that the treatment of elements of geochemical interest, such as Cl, U, and Au, is only possible if a solid host for the element is stable.

The presence of the soluble components in the stable solid phases of a system is a necessary, but not sufficient condition, for the feasibility of lagged speciation. The sufficient condition relates to the manner in which chemical potentials are determined from the linearized formulation of the Gibbs energy minimization problem (Connolly, 2009). This relationship is not easily explained, so it may be helpful to note that the most important manifestation of the sufficient condition is that lagged speciation fails if the number of compositional degrees of freedom associated with the fluid phase increases during iteration. Thus, lagged speciation will fail for any bulk composition that lies within the two-phase fields of the CaO–SiO_2–H_2O phase diagram (Fig. 1b) and, in phase diagram sections as a function of pressure and temperature, the failure condition usually coincides with a phase boundary across which the number of solid phases decreases.

In painful detail, the origin of the sufficient condition is that in successive linear programming the possible compositional variation of any phase is discretized, and the discrete states are treated as individual phases in the internal representation of the problem. Consequently, any stable phase assemblage is represented internally as an invariant assemblage consisting of as many discrete states as the system has components. If the true variance of the phase assemblage is greater than zero, then the internal representation must include more than one discrete composition of a

Table 1

Mineral notation, formulae and solution model sources (1 – Green et al., 2016; 2 – Holland and Powell, 1998; 3 – Fuhrman and Lindsley, 1988; 4 – Chatterjee and Froese, 1975; 5 – Green et al., 2007). Abbreviations for non-stoichiometric phases are capitalized. See Appendix for condensed phase and fluid species thermodynamic data sources.

Symbol	Solution	Formula	Source
Amph	clinoamphibole	$Ca_{2(y+u+v)}Na_{u+2(w+z)}[Mg_xFe_{1-x}]_{7-3u-2v-4(w+z)}Fe_{2z}Al_{4y+3v+2w}Si_{8-(y+v)}O_{22}(OH)_2$	1
als	aluminosilicate	Al_2SiO_5	
arag	aragonite	$CaCO_3$	
cc	calcite	$CaCO_3$	
coe	coesite	SiO_2	
Cpx	clinopyroxene	$[Na_{y+w}Ca_{1-y-w}][Fe_{1-x-y}Mg_xAl_y]Si_2O_6$	5
Dol	dolomite	$CaMg_xFe_{1-x}(CO_3)_2$	2
F	fluid		
Fsp	feldspar	$K_yNa_xCa_{1-x-y}Al_{2-x-y}Si_{2+x+y}O_8$	3
Grt	Garnet	$[Fe_xCa_yMg_{1-x-y}]_3[Fe_{1-v}Al_v]_2Si_3O_{12}$	1
ky	kyanite	Al_2SiO_5	
law	lawsonite	$CaAl_2Si_2O_6(OH)_2$	
lm	lime	CaO	
M	magnesite	$Mg_xFe_{1-x}CO_3$	2
Mlt	melt		
Ms	mica	$K_xNa_{1-x}[Mg_{1-v}Fe_v]_yAl_{3-y}Si_{3+y}O_{10}(OH)_2$	4
mu	muscovite	$KAl_3Si_3O_{10}(OH)_2$	1
Pu	pumpellyite	$Ca_4Mg_xFe_{1-x}[Fe_yAl_{1-y}]_5Si_6O_{21}(OH)_7$	ideal
q	quartz	SiO_2	
san	sanidine	$KAlSi_3O_8$	
stlb	stilbite	$CaAl_2Si_7O_{11}(OH)_{14}$	
Stlp	stilpnomelane	$K_{0.5}[Mg_{1-x}Fe_x]_5Al_2Si_8O_{18}(OH)_{12.5}$	ideal
stv	stishovite	SiO_2	
wo	wollastonite	$CaSiO_3$	

stable phase. These internal phases are homogenized to form the true phases of the final result. The maximum number of internal phases that may represent a single true phase is equal to the number of independently variable components in the phase (Connolly, 2009). In the case of back-calculated speciation, soluble components in the fluid phase are not independently variable because they are determined by the coexisting solids; therefore, the maximum number of internal phases that may represent the fluid in any given assemblage is equal to the number of solvent components. In the $CaO-SiO_2-H_2O$ example, as the solids possess no compositional degrees of freedom and the solvent has only one component, it is impossible to represent a phase assemblage of $<c = 3$ phases. Thus, lagged speciation becomes infeasible during iteration for bulk compositions that lie within the wo + F phase field even though both solute components are present in wollastonite.

The $CaO-SiO_2-H_2O$ example is potentially misleading in that the relationship between feasibility and variance is specific to the case illustrated. There is no such relationship in general. However, because any stable phase assemblage is represented internally by an invariant set of discrete phase states, the example illustrates a general relationship between the bulk composition and the solid- and fluid-saturation surfaces. Specifically, that the probability of specifying an infeasible bulk composition approaches zero in the limit that the bulk composition nears the fluid-saturation surface and approaches unity in the limit that the bulk composition nears the solid-saturation surface.

Two calculations illustrate the manifestation of infeasibility conditions quantitatively (Fig. 2, see the Appendix for thermodynamic details). For a system composed of 1 kg H_2O + 10 mol SiO_2 (Fig. 2a) the infeasibility conditions map the solid-saturation surface as a function of pressure and temperature. The maximum in Si-solubility at high pressure and intermediate temperature reflects the dominance of ionic species ($HSiO_3^-$) at low temperature and molecular species (SiO_2, Si_2O_4) at high temperature (Manning et al., 2010; Sverjensky et al., 2014). The change in solubility mechanism has the consequence that the high-temperature solid-saturation surface coincides with the 1 molal Si-isopleth for the fluid, whereas the low temperature solid-saturation surface lies at slightly higher Si-molality because the formation of H-bearing so-

lute species reduces the mass of the solvent species (H_2O). The system composed of 20 mol H_2O + 12 mol SiO_2 + 0.5 mol K_2O + 1 mol Al_2O_3 (Fig. 2b) illustrates a case where the necessary condition for feasibility is insufficient, in that all soluble components are present in the stable solids at the limit of the feasible conditions. In this example, the limit of feasible conditions coincides with the low pressure boundary of the mu + q + F phase field, analogous to the wo + F field in the schematic $CaO-SiO_2-H_2O$ example (Fig. 1b). That lagged speciation is feasible in the high-variance melt phase fields (Mlt + q + F and Mlt + F) demonstrates that the sufficient condition for feasibility is not directly related to phase field variance. Both examples demonstrate that even in relatively fluid-rich systems, simple back-calculation may provide accurate solubility estimates and therefore that the chief benefit of lagged speciation is that it automatically defines phase changes caused by solubility.

Although the necessary condition for feasibility is redundant in light of the sufficient condition, the necessary condition has been discussed because its chemical significance is evident. The conditions for algorithmic feasibility illustrate problems that arise in fluid-rich systems and raises the question of whether the rock-dominated limit of Galvez et al. (2015) can be usefully defined. From a phase equilibrium perspective, the only robust formulation of this limit identifies it as the fluid-saturation surface, i.e., the conditions at which fluid is stable, but its amount is zero. As such the limit is unduly restrictive and has no practical utility other than to indicate that back-calculation is likely to be accurate if the fluid mass is small. An alternative formulation of the rock-dominated limit adopted here is that it corresponds to the conditions at which lagged speciation becomes infeasible. Within this limit the lagged speciation algorithm is unconditionally stable.

4. Devolatilization of subduction zone sediment

To provide a minimal model for subduction zone devolatilization the geotherm (Fig. 3) adopted here represents subduction of a young (40 Ma) slab at a rate of 10 cm/y and a kinematically prescribed dip of 45° (Rupke et al., 2004). Comparison to the compilation of Syracuse et al. (2010) suggests that the model sub-arc temperatures are close to the lower limit of plausible subduction

(a)

(b)
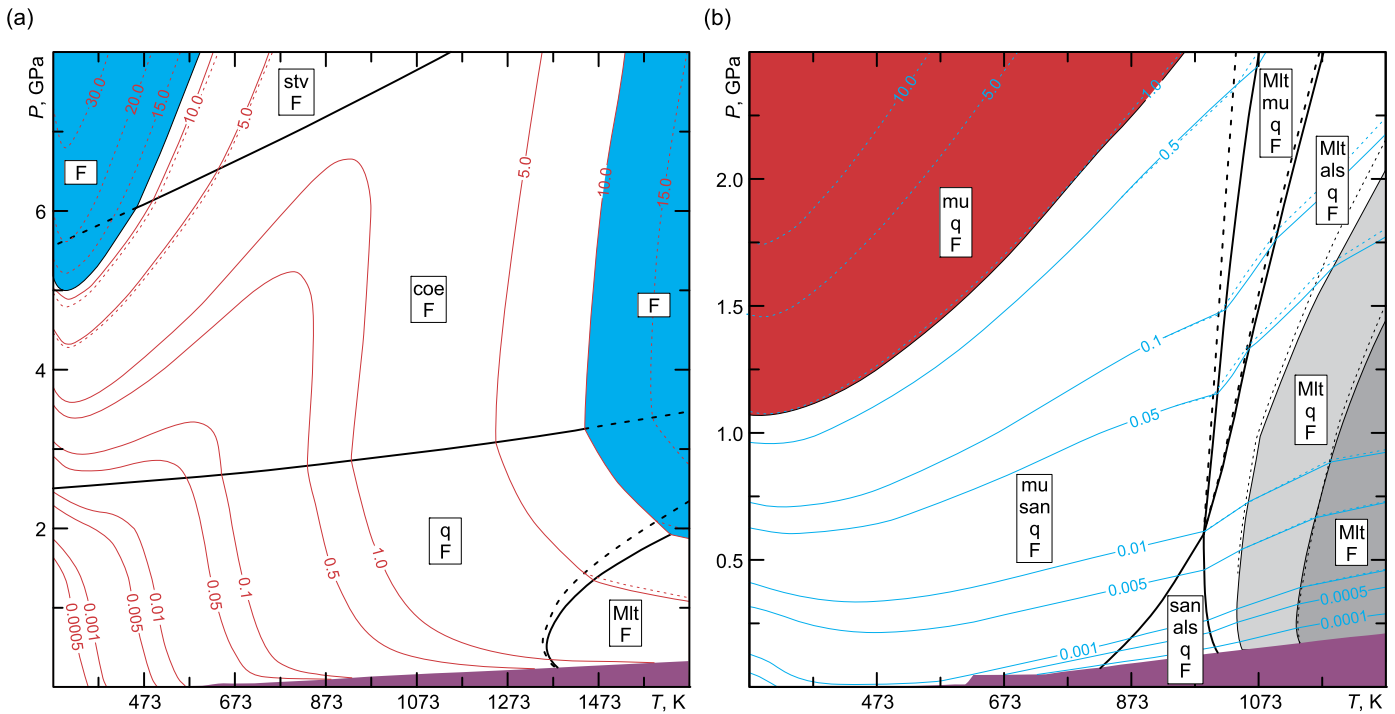
Fig. 2. Phase relations calculated as a function of pressure and temperature by lagged speciation for systems composed of (a) 1 kg H_2O + 10 mol SiO_2 and (b) 20 mol H_2O + 12 mol SiO_2 + 0.5 mol K_2O + 1 mol Al_2O_3 (see Table 1 for phase notation and the Appendix for thermodynamic details). Heavy solid black lines locate univariant phase fields and thin black solid lines locate the boundaries of high variance phase fields, gray-scale shading indicates high variance phase fields mapped by lagged speciation. The boundaries of the red (mu + q + F) and blue (F) phase fields are defined by lagged speciation, but the algorithm is infeasible within these fields. Blue shading indicates that infeasibility can be established, in this case trivially, from the necessary condition that the condensed phases contain all the non-solvent components of the system. The blue/red color coding has the same significance as in Fig. 1c. The condition for infeasibility is sensitive to both the fluid mass and solute concentrations; solute concentration cannot be independently controlled, but a reduction in solvent mass expands the range of feasible calculation. The magenta field indicates the conditions of vapor or vapor-like fluid densities at which the HKF formalism is not fully parameterized and does not extrapolate plausibly (Shock et al., 1992). Solid red and blue contours indicate, respectively, total Si and K molality in the fluid as computed by lagged speciation. Dashed curves and contours indicate phase boundaries and results obtained by simple back-calculation. Simple back-calculation assumes the solute-free phase relations (e.g., as in Fig. 1a) and can be done regardless of feasibility conditions. Thus the back-calculated solubility isopleths in the infeasible lagged speciation phase fields are for phase assemblages (coes/stv + F in (a) and mu + san + q + F) that do not satisfy the mass balance constraints of the system.
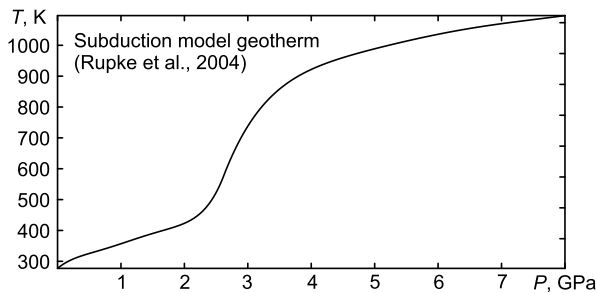
Fig. 3. Geotherm conditions assumed for the subduction zone models (Rupke et al., 2004).

zone conditions. As low temperature favors the electrolytic solubility mechanism, the choice of a cool geotherm provides a best case scenario for the importance of electrolytic solutes during subarc decarbonation. Sediment lithologies are heterogeneous; rather than consider this compositional spectrum, the global average marine sediment (GLOSS; Plank and Langmuir, 1998) composition is taken to be representative (Table 2). Previous phase equilibrium modeling (Kerrick and Connolly, 2001a) indicates that the high GLOSS water-content favors decarbonation at low temperature compared to water-poor carbonate sediments. Because the GLOSS average does not quantify the redox state of iron or carbon, the initial bulk oxygen content is computed under the assumption that all iron is ferrous and all carbon is present as carbonate, a configuration identified here as the neutral bulk redox state. In the resulting models, the stability of ferric iron in low-temperature

Table 2

Average subducted sediment composition (GLOSS, Plank and Langmuir, 1998). The GLOSS composition has been modified by the addition of sulfur corresponding to the presence of ~0.1 volume % pyrite, the original O_2-content has been recomputed so that the bulk composition is redox neutral. The metasediment composition is the bulk composition obtained at 4.3 GPa from the GLOSS composition by open-system devolatilization (Fig. 6c).

	Initial GLOSS sediment		Metasediment at 4.3 GPa	
	mass fraction (%)	mol/kg	mass fraction (%)	mol/kg
H_2	0.823	4.085	0.197	0.978
C	0.824	0.686	0.847	0.706
Si	27.621	9.835	29.317	10.439
Al	6.369	2.360	6.802	2.521
Fe	4.112	0.736	4.392	0.786
Mg	1.520	0.625	1.623	0.668
Ca	4.285	1.069	4.551	1.135
Na	1.809	0.787	1.804	0.785
K	1.735	0.444	1.798	0.460
O_2	50.578	15.806	48.322	15.101
S_2	0.323	0.101	0.345	0.108

minerals has the consequence that a small amount of carbonate is reduced to form graphite at surface conditions and graphite or diamond persists, except in infiltration models, as a stable phase at all conditions. Preliminary calculations demonstrated that an implausible initial ferric/ferrous ratio of ~2.5 would be necessary to completely suppress the stability of reduced carbon during devolatilization. At the opposite extreme, essentially all the initial carbon must be reduced to destabilize carbonate. This extreme leads to dramatically different devolatilization behavior in that at

low pressures ($<\sim$1.5 GPa) almost all carbon is released in the form of a methane-rich fluid, an effect that may be of some interest but effectively eliminates decarbonation as a mechanism for explaining island-arc carbon emissions. These considerations suggest that predictions based on the neutral bulk redox state initial condition are likely to be characteristic of natural conditions and, to a first approximation, account for the presence of organic carbon in marine sediments (Bebout, 1995).

Sulfur is an important, but oft neglected, component of subduction zone volatile budgets (Pokrovski and Dubrovinsky, 2011; Evans et al., 2014; Kagoshima et al., 2015; Canil and Fellows, 2017). To evaluate the effect of Sulfur, the GLOSS composition (Table 2) was modified by the addition of 0.1 mol S_2/kg. The sulfur is presumed to be accommodated in pyrite ($\sim$0.6 vol.%) and the bulk oxygen content reduced accordingly, i.e., the bulk molar O_2 content is reduced by half the molar S_2 content. The possibility of the presence of oxidized sulfur in the initial bulk composition was not considered because in preliminary calculations sulfates were not predicted to coexist with graphite + carbonate at surface conditions.

The HKF/DEW data base (Shock et al., 1992; Sverjensky et al., 2014) includes 28 C–O–H–S solute species. In initial calculations the concentrations of glycolate ($C_2H_3O_3{}^-$), glutarate ($C_5H_7O_4{}^-$), and lactate ($C_3H_5O_3{}^-$) were implausibly high at all conditions of interest. Accordingly, these species were excluded from all subsequent calculations. In mixed-volatile solvent calculations (the COHS-solvent model), none of the HKF/DEW C–O–H–S organic and/or molecular solute species were considered, and the solvent was initially treated as a mixture of H_2O, H_2, CO, CO_2, CH_4, SO_2, and H_2S species. These calculations demonstrated that H_2, CO, CH_4, and SO_2 had no significant effect on solute speciation or bulk chemistry. The final calculations considered only the four dominant solvent species (H_2O, CO_2, CH_4, and H_2S).

Results are presented for closed-system sediment devolatilization computed by lagged speciation with the COHS-solvent model. These results are compared to four variants to illustrate technical differences and to inform understanding of the devolatilization process. Specifically, the variants, and their purposes, are: 1) simple back-calculation, to contrast the lagged- and back-calculation methods; 2) H_2O-solvent, to illustrate the consequences of the choice of solvent model on fluid speciation and chemistry; 3) fluid-fractionation, a more realistic open-system model for devolatilization; and 4) infiltration-driven devolatilization, an effective, if poorly constrained, mechanism for slab-decarbonation.

Thermodynamic details of the model calculations and the implementation of the HKF/DEW formulation are summarized in the Appendix. The computer program and data files used for these calculations are available at www.perplex.ethz.ch/perplex_electrolyte.html.

4.1. Devolatilization vs dissolution

The difference between the phase proportions predicted for GLOSS subduction models that account for both devolatilization and dissolution (Fig. 4a) and a model without dissolution (Fig. 4b) is surprisingly large. Most notably in the absence of dissolution white mica undergoes no significant dehydration. In contrast, in the lagged speciation model, mica is almost completely dehydrated at the maximum pressure, 6.6 GPa, of the profile. Likewise, without dissolution, the proportions of pyrite and aragonite are approximately constant after dolomite is destabilized at $\sim$5 GPa, but in the lagged speciation model pyrite and aragonite are eliminated by dissolution at 6.4 GPa. The maximum pressure at which phase relations are computed in the lagged-speciation calculation is the point at which the fluid composition becomes so solute-rich that the rock-dominated limit (Fig. 2) is violated.

Although not easily visible (Fig. 4b), the volume of diamond increases ten-fold, to $\sim$0.1%, over the same interval that aragonite begins to dissolve. From the fluid speciation (Fig. 5a), it is apparent that this phase of diamond precipitation is related to an increase in the concentration of $CaSO_4$ in the fluid, which forms by the reduction of carbon bound in aragonite. This prediction is consistent with the observation of sulfate species and solid carbonate in fluid inclusions in natural subduction zone diamonds (Frezzotti et al., 2011). In calculations not reproduced here, Aragonite and mica are destabilized at essentially the same conditions for the S-free GLOSS composition; therefore, this process is not directly dependent on the stability of aqueous $CaSO_4$ and the oxidation of pyrite.

As anticipated by earlier studies (Manning et al., 2013; Galvez et al., 2015), dissolution roughly doubles carbon-loss during subduction in the best case, cool-subduction, scenario considered here (Fig. 6a). In early models of slab-decarbonation (Kerrick and Connolly, 2001a, 2001b), closed-system results were used to estimate carbon-transfer under the assumption that the accumulated fluid is released in a single batch at sub-arc depth. On a global scale the fluid-mediated mass transfer of element i is

$$Q_i = v_s h_0 \rho_0 N_i n_i \tag{13}$$

where v_s is the global subduction rate (2.7 km^2/y; Plank and Langmuir, 1998), h_0 and ρ_0 are initial thickness and density of the source rock, N_i is the atomic weight, and n_i is the number of moles of element released by a unit mass of the source rock (Fig. 6a). For present purposes, it is assumed that the bulk of the slab carbon is contained in a 1300 m thick section consisting of 800 m of GLOSS sediment (Plank and Langmuir, 1998) and 500 m of hydrothermally altered basalt (Staudigel et al., 1989). Both lithologies have comparable initial carbon-content (0.7 mol/kg) and density (2600 ± 100 kg/m^3) in which case the carbon input by subduction of oceanic crust is 76 Mt/y, which lies within the range of recent estimates (35–88 Mt/y; Kerrick and Connolly, 2001a; Dasgupta and Hirschmann, 2010; Kelemen and Manning, 2015). To make a first order assessment of the global carbon-loss, it is assumed that carbon-loss in the basalt section is comparable to that computed for GLOSS sediment. Justification for this assumption follows from the mineralogical similarity of sedimentary and basaltic eclogites (Kelemen and Manning, 2015). Based on these assumptions the global carbon-loss for batch devolatilization with ($n_C = 0.28$ mol/kg, Fig. 6a) and without ($n_C = 0.12$ mol/kg) dissolution is, respectively, 30.6 Mt/y and 13.1 Mt/y, these values compare with estimates of island-arc carbon emissions (18–55 Mt/y; Kerrick and Connolly, 2001a; Dasgupta and Hirschmann, 2010; Kelemen and Manning, 2015). At face value, this result suggests dissolution resolves the mismatch between carbon loss predicted by the closed-system model and observed carbon emission. That conclusion is not justified in light of model uncertainty. Typical sub-arc temperatures may exceed those estimated here by $\sim$100 K (Syracuse et al., 2010). Such an increase in sub-arc temperature would increase molecular CO_2 solubility five-fold (Connolly, 2005). While electrolytic chemistry would moderate this increase it is likely that such thermal effects dwarf the effect of dissolution (Galvez et al., 2016). Thus the criticism that closed-system devolatilization models are incapable of explaining island-arc carbon emissions is misplaced. The legitimate criticism of closed-system models for assessing carbon-loss is that the implied batch mechanism for fluid release is physically implausible.

Although the closed-system model does not provide a realistic basis for assessment of slab-mantle mass transfer during subduction, such models generally provide an upper limit for mass transfer effected without the infiltration of externally derived fluids
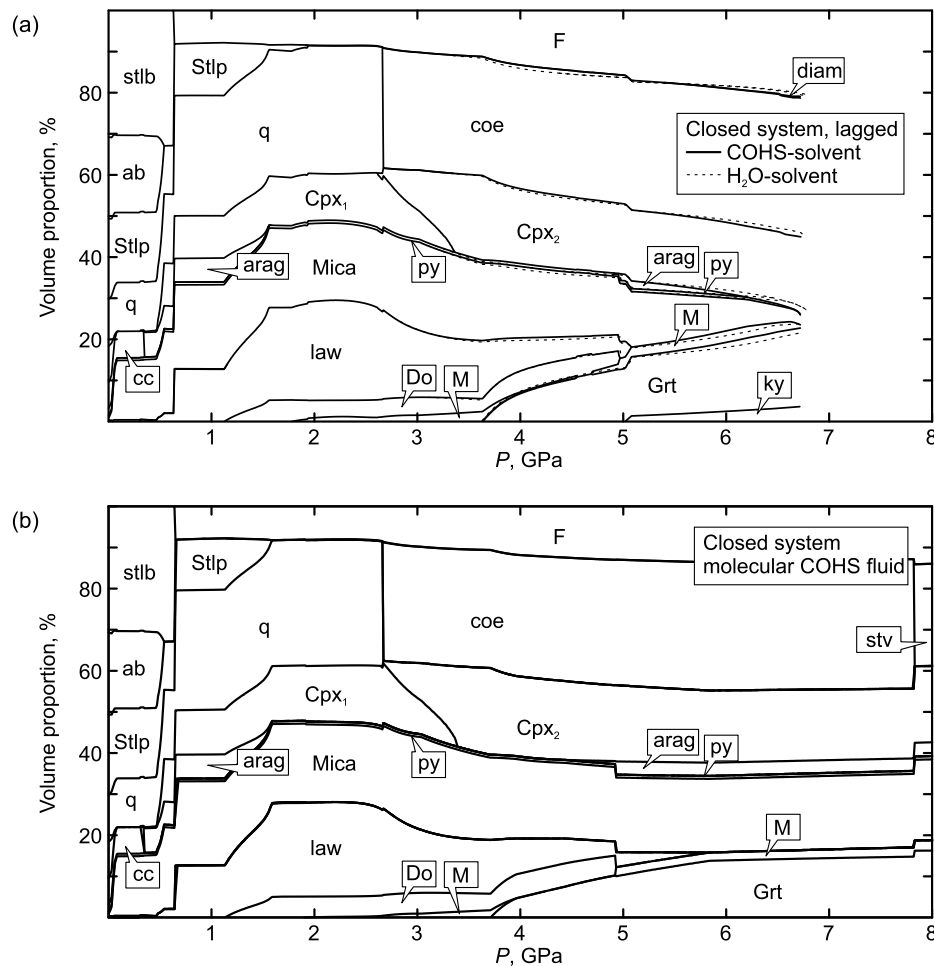
Fig. 4. Volumetric phase proportions during closed-system devolatilization of the GLOSS sediment composition (Table 2) computed by (a) lagged speciation and (b) without taking into account dissolution. The lagged speciation results compare the COHS-solvent model (solid curves) and the H_2O-solvent model (dashed curves) commonly assumed in applications of the HKF/DEW formalism. The fields for small amounts of graphite, potassium feldspar, clinoamphibole, and pumpellyite, which are stable at low pressure, are not labeled. Mineral proportions (not shown) computed for the open-system devolatilization model are essentially identical to those obtained by neglecting dissolution. Phase notation and solution models are summarized in Table 1.

(Kerrick and Connolly, 2001b). As such, the closed-system model suggests that devolatilization processes have the potential to deplete K, H and S from subducted sediments, and almost no capacity to effect Fe or Al mass transfer. The immobility of Al is at odds with experimental observation (e.g., Tsay et al., 2017) and may merely reflect the current limitations of the solute-species model (Manning, 2007; Manning et al., 2010).

4.2. Simple back-calculated vs lagged speciation

Simple back-calculated speciation (Galvez et al., 2015) assumes the mineralogy and solvent chemistry obtained by a solute-free phase equilibrium model (e.g., Fig. 4b), as such the simple back-calculated model cannot account for the effects of dissolution on mineral stability. However, it is appropriate to compare the lagged and back-calculated fluid speciation to assess the accuracy of back-calculation as an approximation of fluid chemistry. This comparison (Fig. 5a) is reassuring in that, at conditions within the rock-dominated regime (i.e., pressure <6.7 GPa), the simple back-calculated speciation is generally accurate to within a factor of two or better. Thus, the only prominent disadvantage of simple back-calculation is that it provides no means of recognizing the conditions at which the assumption of a rock-dominated regime is invalid.

4.3. H_2O- vs COHS-solvent

Comparison of phase equilibria computed for the H_2O- and COHS-solvent models (Fig. 4a, Fig. 5b, Fig. 6b) reveals only minor differences. Both models predict CO_2 as the only major C–O–H–S species (Fig. 5b). Of the 25 C–O–H–S solute species considered in the H_2O-solvent model, but excluded from the COHS-solvent model, only formate ($HCOO^{2-}$) is predicted to be stable at concentrations in excess of 10^{-2} m, a prediction consistent with the observation of abiotic formate as a prominent species in sea-floor hydrothermal systems (Lang et al., 2018). Although no molecular C–O–H–S solute species were included in the COHS-solvent calculation, the use of a mixed-volatile solvent model does not preclude the simultaneous treatment of molecular volatile solute species.

From a computational perspective the advantage of the H_2O-solvent model is that it is inexpensive and accurate in the limit of dilute molecular solute concentrations. The chief disadvantage of the model is that it cannot be used predict phase separation, for example, the coexistence of H_2O- and CH_4- or CO_2-rich fluids (Fruh-Green et al., 2004). The availability of molecular equations makes the prediction of phase separation for mixed-volatile solvents possible; however, in practice, extrapolation of the HKF/DEW formulation to treat non-aqueous solvents is largely untested.
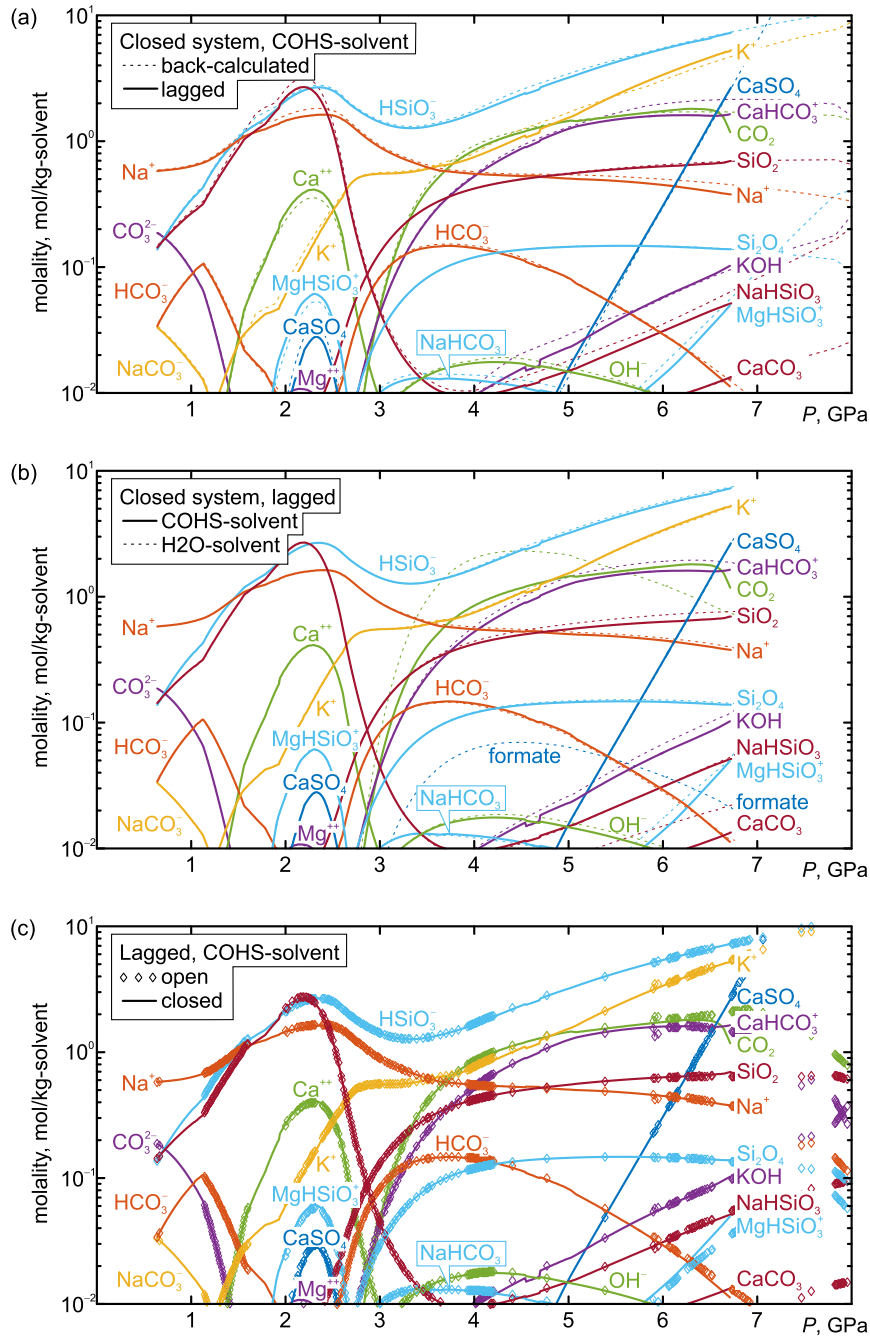
Fig. 5. Fluid speciation in various models for the devolatilization of the GLOSS sediment composition. (a) Closed-system devolatilization with the COHS-solvent model, comparing the lagged (solid curves) and simple back-calculated (dashed curves) speciation. (b) Closed-system devolatilization using lagged speciation, comparing the COHS- (solid curves) and H_2O-solvent (dashed curves) models. (c) COHS-solvent using lagged speciation, comparing open- (diamond symbols) and closed-system (solid curves) devolatilization. In simple back-calculation, fluid speciation is calculated post-hoc from the solute-free phase equilibrium model (Fig. 4b), thus the phase proportions and fluid composition violate mass balance. Nonetheless, the back-calculated speciation is accurate to within a factor of two within the rock-dominated limit (i.e., at pressure $< \sim 6.7$ GPa).

4.4. Open- vs closed-system devolatilization

The open-system model corresponds to Rayleigh fractionation of the fluid phase. This simulates a scenario in which fluid generated by sediment devolatilization is lost immediately to the mantle wedge and that the sediments are isolated from any fluids produced at greater depth by channelized flow. The mass-loss for this model (Fig. 6c) is roughly an order of magnitude below the solute mass present in the fluid for the closed-system model (Fig. 6a), yet the fluid speciation of both models is nearly identical (Fig. 5c). The prominent differences in bulk fluid chemistry between the two

models arise because in the open system mass-loss to the fluid is irreversible, whereas in the closed system the components of the fluid may reprecipitate as solids (e.g., Si, K, and C). As most fluid generation occurs at low pressure this behavior has the consequence that the open-system mass-loss reflects low pressure solubilities and is dominated by Na and, to a lesser extent Si and carbonate species. That mica is refractory in the open-system model demonstrates that its dehydration in the closed-system model is due entirely to dissolution.

The lagged fluid speciation in the closed- and open-system models is virtually identical (Fig. 5c) at pressures below the rock-
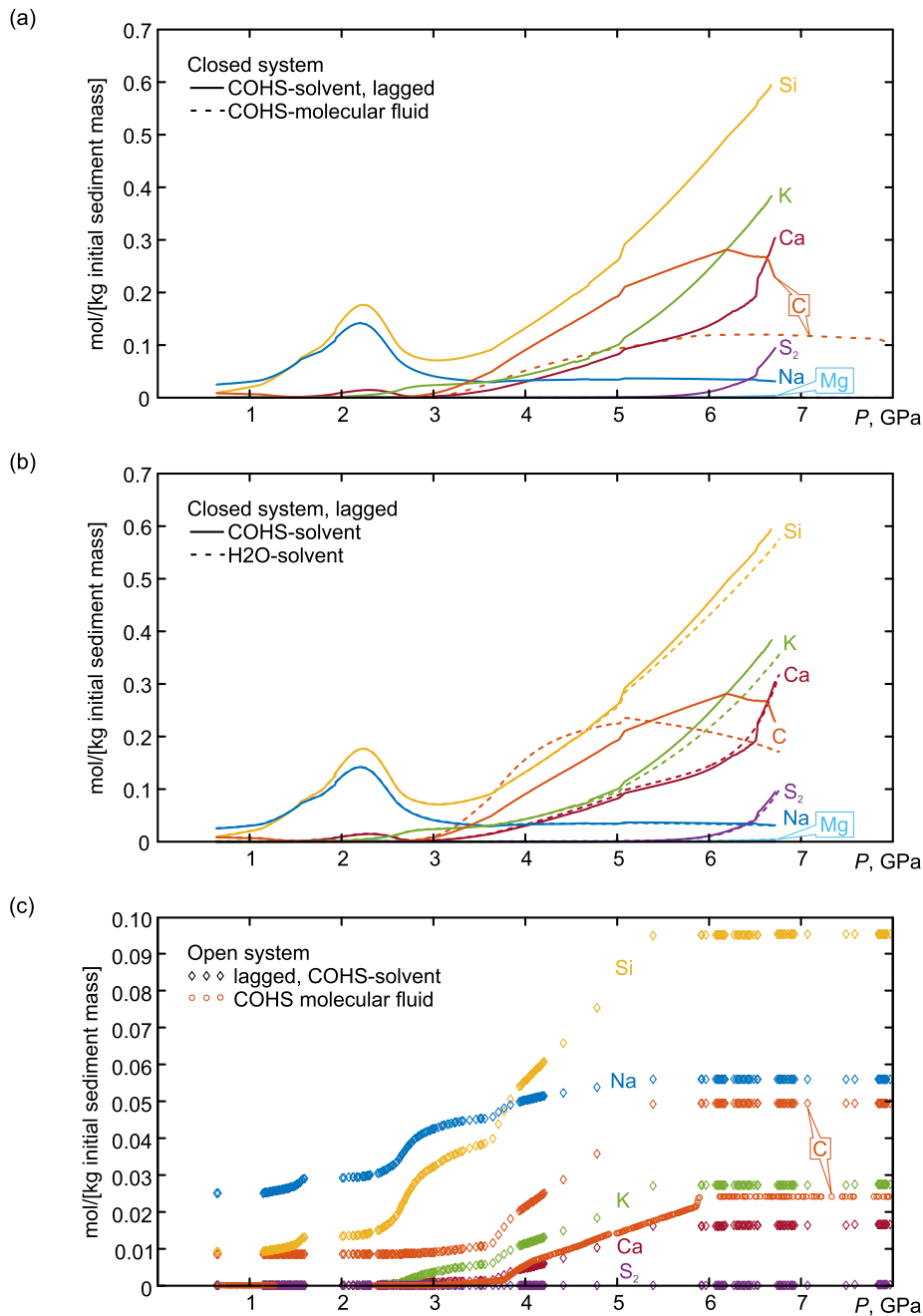
Fig. 6. Mass present in, or removed by, the fluid generated during devolatilization of 1 kg of GLOSS sediment in various models. (a) Closed-system: COHS-solvent, lagged speciation (solid curves) vs COHS molecular fluid (dashed curve for C). (b) Closed-system, lagged speciation: COHS-solvent (solid curves) vs H₂O-solvent (dashed curves). (c) Open-system: COHS-solvent (diamond symbols) vs COHS molecular fluid (circular symbols for C); symbols indicate the points along the subduction path at which fluid was generated. In closed-system models, the mass of a component present in the fluid may decrease with pressure due to changing solubility; in the open-system model, mass loss is irreversible.

dominated limit for the closed-system model (∼6.7 GPa). The open-system model does not reach this limit because the removal of sulfur from the system stabilizes the calculation. Comparison of the open-system fluid speciation with that obtained by back-calculation (Fig. 5a) illustrates that use of back-calculated results beyond the rock-dominated limit leads to substantial errors.

By excluding the possibility of fluid infiltration, the open-system model represents the most conservative model for sub-duction zone mass transfer. Based on the assumptions discussed previously in reference to the closed-system model, Eq. (13) yields global carbon losses by fluid fractionation ($n_C = 0.05$ mol/kg, Fig. 6c) of 5.5 Mt/y, of which 1.1 Mt/y is lost at fore-arc depths at the onset of fluid generation. While the uncertainties are

formidable, this result suggests that indeed a simple devolatiliza-tion-dissolution process cannot explain island-arc carbon emis-sions in the range 18–55 Mt/y (Kerrick and Connolly, 2001a; Dasgupta and Hirschmann, 2010; Kelemen and Manning, 2015) and that a fluid-mediated explanation for these emissions requires that the crust be infiltrated by fluids derived by mantle dehydra-tion.

4.5. Infiltration-driven devolatilization

For the subduction zone thermal model adopted here (Rupke et al., 2004), serpentine dehydration in the subducted mantle oc-curs when the slab surface is at 3.9–4.6 GPa (Connolly, 2005).
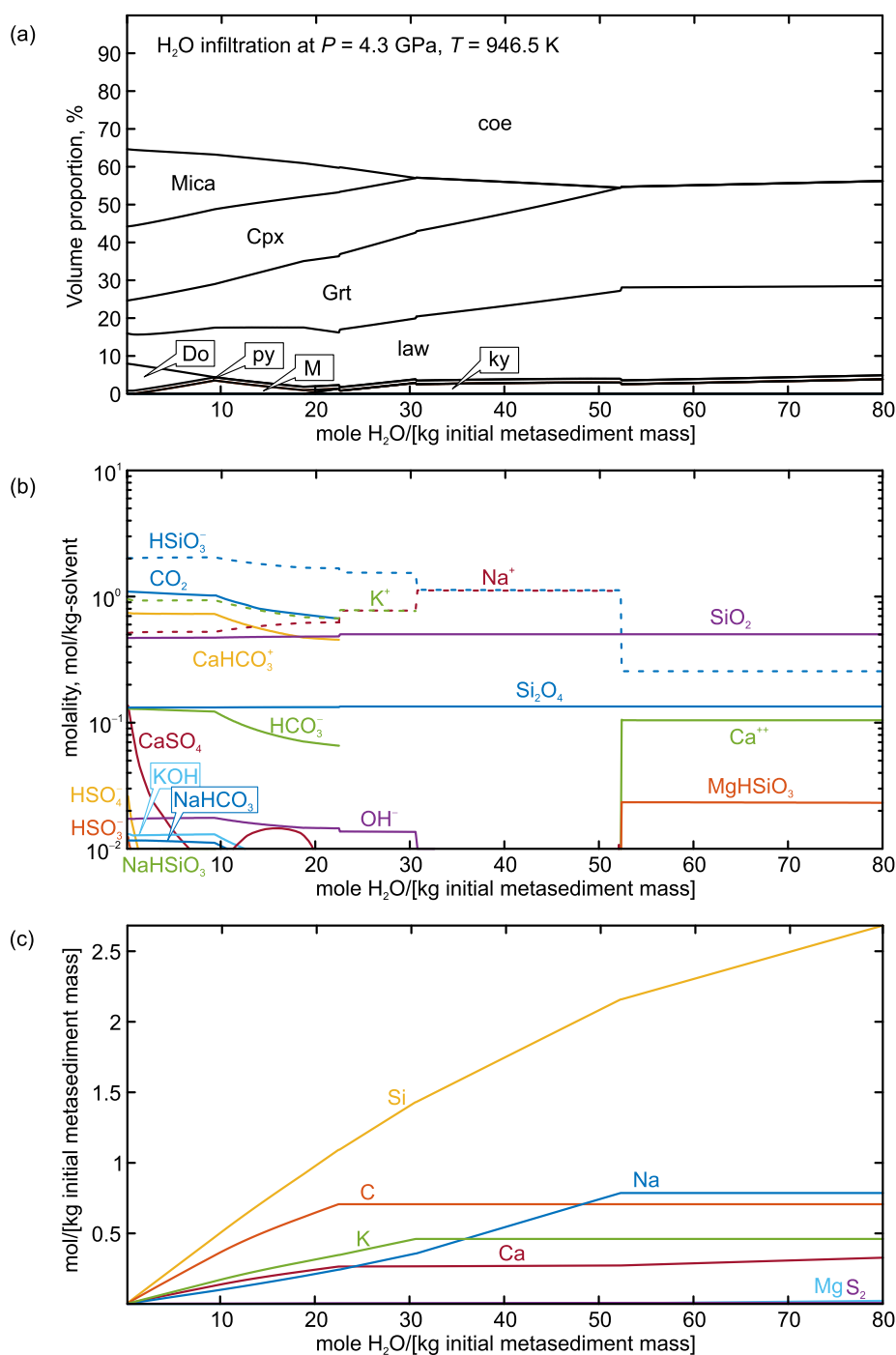
Fig. 7. Phase proportions (a), fluid speciation (b), and mass loss (c) for the infiltration-driven devolatilization model. Phase notation and solution models are summarized in Table 1.

Taking 4.3 GPa as a representative pressure and the metasediment composition obtained from the open-system model at that condition (Table 2), infiltration-driven mass transport is assessed under the assumption that fluid released by serpentine dehydration is, and remains, pure water until it reaches the sediments. This assumption is unlikely to be true for elements such as Na and Si (Galvez et al., 2016), which are abundant in the igneous crust, but it is a reasonable first approximation for K and C which are concentrated in the thin (∼1300 m) package of altered basalt and sediment atop the subducted slab (Staudigel et al., 1989; Alt and Teagle, 1999). The thinness of this package is taken as justification for reducing the problem to a zero-dimensional model.

Models in which the fluid is generated within, and infiltrates through, a subducted metamorphic column are tractable (Connolly, 2005; Gorman et al., 2006), but too complex for presentation here.

The initial fluid speciation in the zero-dimensional infiltration model (Fig. 7b) is slightly different from the speciation for the open-system model (Fig. 5c) at the same pressure because the addition of pure water eliminates the small amount of diamond that is ubiquitous in the previous models and stabilizes oxidized sulfur species ($CaSO_4$, HSO_4^-, HSO_3^-). The infiltration model indicates that ∼23 mol of water is required to completely decarbonate a kilogram of GLOSS metasediment (Fig. 7c). As serpentinized mantle

contains ~13 wt % H_2O or 7.2 mol H_2O/kg mantle, this implies a mass of serpentinite ~3.2 times that of the carbon-bearing oceanic crust is adequate to completely decarbonate the crust. This mass is well within estimates for upper limit on the extent of mantle serpentinization (Connolly, 2005).

The elimination of mica and alkali earth elements by the addition of slightly more water than required for decarbonation leaves lawsonite as the only carrier of water at depths beyond the conditions of serpentine dehydration. With continued subduction lawsonite would dehydrate (Fig. 4), leaving the metasediment completely depleted in alkali earth elements, and hydrogen and, thereby, refractory to melting. By neglecting the effect of the igneous crust on the chemistry of mantle derived fluid, the present model likely exaggerates Na-depletion. This model defect is less likely to be important for potassium, which correlates strongly with hydrogen, because of its greater solubility and lower absolute abundance in the igneous crust. Thus, the result suggests an anti-correlation between the efficacy of infiltration-driven decarbonation and slab melting. Unfortunately, there are many reasons why slab melting (Behn et al., 2011) is sporadic, and therefore its absence is not an argument for the importance of infiltration-driven decarbonation.

The complete depletion of C, K, and Na in the infiltration-driven model may seem to contradict the lagged speciation rock-dominated limit. This is not the case, as in the simple open-system model, because the elements depleted from the condensed phases are removed from the system by the fluid.

5. Discussion

The lagged-speciation algorithm derives extraordinary efficiency by using back-calculated fluid speciation (Galvez et al., 2015) to predict the stable composition of electrolytic fluids during Gibbs energy minimization. The cost of this efficiency is that the algorithm fails if the predicted fluid composition is inconsistent with mass balance constraints. While there is no remedy for this condition, the conditions can be recognized, making it apparent when reformulation of the solvent model or a more rigorous algorithm (e.g.: Harvie et al., 1987; Karpov et al., 2001) is required. A limitation of the algorithm related to this failing is that it cannot treat situations in which an element is present only in the form of a solute species. In the case C, O, H, and S, which appear both as molecular fluid species and common mineral constituents, this limitation can be circumvented by reformulating the solvent model to include these elements. Halogens are more problematic. There are equations of state that describe brines in terms of a solvent standard state for NaCl (Driesner and Heinrich, 2007; Aranovich et al., 2010; Dubacq et al., 2013), the complication in integrating such equations of state with solute speciation models such as the HKF is to define a relation between the macroscopic and microscopic NaCl content and to account for the resulting nonlinearity in activity-composition relations. This complication has not been addressed in the computer implementation of the lagged speciation algorithm. An alternative strategy for treating undersaturated solute components is to introduce an auxiliary condition for the solute component mass (Galvez et al., 2016); however, this strategy presumes stability of the fluid phase.

In geochemical implementations of the HKF/DEW formulation, water is the sole solvent and molecular volatiles and organic species are described by a solute standard state. In contrast, Galvez et al. (2015) adopted a solvent standard state for the dominant carbonic volatile species. Both solvent formulations offer advantages in specific situations, in the case of a miscible low-temperature water-rich solvent phase both formulations produce comparable results (Fig. 5b). This agreement deteriorates at higher temperature and, due to the implicit assumption of Henryian behavior in

the solute reference state, leads to underestimation of molecular volatile solubilities (Galvez et al., 2016).

Because the primary concern of this paper is methodological, no attempt has been made to assess the accuracy of the thermodynamic data used for the calculations presented here. This data is subject to significant random sources of error, but a bias toward under-prediction of mineral solubility is inherent in microscopic speciation models due to the existence of unanticipated species (Manning, 2007; Pokrovski and Dubrovinsky, 2011; Manning et al., 2010; Tumiati et al., 2017). Sverjensky et al. (2014) demonstrated that the current data is capable of reproducing experimental solubility data in simple systems at subduction zone conditions; however, in systems with chemistry approaching that of natural rocks, thermodynamic models underestimate the concentrations of Ca, Al, Fe, and Mg by orders of magnitude (Galvez et al., 2015). Although this error is significant, the absolute concentrations of these elements, with the probable exception of Al, is small compared to those of the alkali elements (Tsay et al., 2017).

6. Conclusion

With the aforementioned caveats, accounting for electrolytic fluids does not profoundly change the efficacy of fluid-mediated carbon-loss during subduction based on classical molecular fluid models because carbonic molecular species remain prominent, if not dominant, in electrolytic fluids. The behavior of sulfur is more surprising. At fore-arc conditions S is nearly insoluble and accommodated primarily as H_2S. The present modeling (Fig. 5) suggests that sulfur solubility rises at sub-arc conditions due to the stability of oxidized sulfur species that form by the reduction of carbonate to diamond (Frezzotti et al., 2011). This rise in solubility is intriguing as a mechanism for transferring an oxygen excess to the mantle wedge.

Subduction zone carbon input and output are of the same order of magnitude, but are uncertain by at least a factor of two (Kerrick and Connolly, 2001a; Dasgupta and Hirschmann, 2010; Kelemen and Manning, 2015). Thus, there is no compelling argument that slabs must be completely decarbonated at sub-arc depths. A more important issue is whether it is possible to reject the null hypothesis that sub-solidus decarbonation is adequate to explain island-arc carbon emissions. Earlier studies based on a closed-system devolatilization model (Kerrick and Connolly, 2001a, 2001b), which exaggerates the extent of decarbonation, rejected the null hypothesis. Since that time, sub-arc temperature estimates have increased significantly (Syracuse et al., 2010; Penniston-Dorland et al., 2015) with the result the physically unrealistic closed-system model can explain island-arc carbon emissions (Section 4.1). Open-system devolatilization (Section 4.4), the simplest possible physically realistic model, reduces the extent of decarbonation by an order of magnitude, so that it remains plausible to reject the null hypothesis.

The intent here has not been to deny or advocate any particular alternative decarbonization hypothesis, but solely to reexamine the efficacy of sub-solidus infiltration-driven devolatilization. Gorman et al. (2006) is often cited to support the contention that infiltration-driven devolatilization is incapable of explaining island-arc carbon emissions. However, the behavior in the Gorman et al. (2006) models was influenced by the choice of an anomalously young slab age. Because the top of subducted slabs is heated rapidly after the slab mantle becomes detached from the lithosphere (Rupke et al., 2004), carbon solubility rises to a maximum at sub-arc depth for typical subduction zone conditions (Connolly, 2005; Galvez et al., 2016; Fig. 6 here). Slab age is important in this context because it controls when serpentine dehydration, the putative source of infiltrating fluid, is released. For subduction models based on a slab age close to the global average, there is no dif-

ficulty in explaining island-arc carbon emissions in terms of an infiltration-driven scenario for decarbonation (Connolly, 2005). The concern over whether such models are capable of quantitatively explaining decarbonation is misplaced. Rather, the weakness of the infiltration-driven scenario is the assumption that large volumes of mantle-derived fluid equilibrates pervasively with the subducted crust. The value of incorporating electrolytic fluid chemistry in models of infiltration-driven devolatilization is that it offers a complete geochemical picture of the infiltration process and, thereby, may provide arguments for the rejection or acceptance of the mechanism. In particular, the present modeling (Section 4.5) suggests that any sub-solidus infiltration event capable of depleting carbon from the subducted crust would effectively desiccate the crust by potassium depletion and render it refractory with respect to melting. A critical assumption in this argument is that lawsonite is not stable on the fluid-absent solidus (cf., Poli, 2015).

Acknowledgements

Appendix A. Supplementary material

Supplementary material related to this article can be found online at https://doi.org/10.1016/j.epsl.2018.08.024.

References

Ague, J.J., Nicolescu, S., 2014. Carbon dioxide released from subduction zones by fluid-mediated reactions. Nat. Geosci. 7, 355–360. https://doi.org/10.1038/ngeo2143.

Alt, J.C., Teagle, D.A.H., 1999. The uptake of carbon during alteration of oceanic crust. Geochim. Cosmochim. Acta 63, 1527–1535.

Aranovich, L.Y., Zakirov, I.V., Sretenskaya, N.G., Gerya, T.V., 2010. Ternary system $H_2O–CO_2–NaCl$ at high T–P parameters: an empirical mixing model. Geochem. Int. 48, 446–455. https://doi.org/10.1134/s0016702910050022.

Bebout, G.E., 1995. The impact of subduction-zone metamorphism on mantle-ocean chemical cycling. Chem. Geol. 126, 191–218.

Behn, M.D., Kelemen, P.B., Hirth, G., Hacker, B.R., Massonne, H.J., 2011. Diapirs as the source of the sediment signature in arc lavas. Nat. Geosci. 4, 641–646. https://doi.org/10.1038/ngeo1214.

Bethke, C.M., 1996. Geochemical Reaction Modeling: Concepts and Applications. Oxford University Press Inc, New York.

Canil, D., Fellows, S.A., 2017. Sulphide–sulphate stability and melting in subducted sediment and its role in arc mantle redox and chalcophile cycling in space and time. Earth Planet. Sci. Lett. 470, 73–86. https://doi.org/10.1016/j.epsl.2017.04.028.

Chatterjee, N.D., Froese, E., 1975. A thermodynamic study of the pseudo-binary join muscovite–paragonite in the system $KAlSi_3O_8–NaAlSi_3O_8–Al_2O_3–SiO_2–H_2O$. Am. Mineral. 60, 985–993.

Connolly, J.A.D., 2005. Computation of phase equilibria by linear programming: a tool for geodynamic modeling and its application to subduction zone decarbonation. Earth Planet. Sci. Lett. 236, 524–541.

Connolly, J.A.D., 2009. The geodynamic equation of state: what and how. Geochem. Geophys. Geosyst. 10. https://doi.org/10.1029/2009gc002540.

Dasgupta, R., Hirschmann, M.M., 2010. The deep carbon cycle and melting in Earth's interior. Earth Planet. Sci. Lett. 298, 1–13. https://doi.org/10.1016/j.epsl.2010.06.039.

Dasgupta, R., Hirschmann, M.M., Withers, A.C., 2004. Deep global cycling of carbon constrained by the solidus of anhydrous, carbonated eclogite under upper mantle conditions. Earth Planet. Sci. Lett. 227, 73–85. https://doi.org/10.1016/j.epsl.2004.08.004.

DeCapitani, C., Brown, T.H., 1987. The computation of chemical equilibria in complex systems containing non-ideal solutions. Geochim. Cosmochim. Acta 51, 2639–2652.

Driesner, T., Heinrich, C.A., 2007. The system $H_2O–NaCl$. Part I: correlation formulae for phase relations in temperature–pressure–composition space from 0 to 1000 degrees C, 0 to 5000 bar, and 0 to 1 X–NaCl. Geochim. Cosmochim. Acta 71, 4880–4901. https://doi.org/10.1016/j.gca.2006.01.033.

Dubacq, B., Bickle, M.J., Evans, K.A., 2013. An activity model for phase equilibria in the $H_2O–CO_2–NaCl$ system. Geochim. Cosmochim. Acta 110, 229–252. https://doi.org/10.1016/j.gca.2013.02.008.

Evans, K.A., Tomkins, A.G., Cliff, J., Fiorentini, M.L., 2014. Insights into subduction zone sulfur recycling from isotopic analysis of eclogite-hosted sulfides. Chem. Geol. 365, 1–19. https://doi.org/10.1016/j.chemgeo.2013.11.026.

Facq, S., Daniel, I., Montagnac, G., Cardon, H., Sverjensky, D.A., 2014. In situ Raman study and thermodynamic model of aqueous carbonate speciation in equilibrium with aragonite under subduction zone conditions. Geochim. Cosmochim. Acta 132, 375–390. https://doi.org/10.1016/j.gca.2014.01.030.

Frezzotti, M.L., Selverstone, J., Sharp, Z.D., Compagnoni, R., 2011. Carbonate dissolution during subduction revealed by diamond-bearing rocks from the Alps. Nat. Geosci. 4, 703–706. https://doi.org/10.1038/ngeo1246.

Fruh-Green, G.L., Connolly, J.A.D., Plas, A., Kelley, D.S., Grobety, B., 2004. Serpentinization of oceanic peridotites: implications for geochemical cycles and biological activity. In: Wilcock, W.S.D., DeLong, E.F., Kelley, D.S., Baross, J.A., Cary, S.C. (Eds.), Subseafloor Biosphere at Mid-Ocean Ridges, pp. 119–136.

Fuhrman, M.L., Lindsley, D.H., 1988. Ternary-feldspar modeling and thermometry. Am. Mineral. 73, 201–215.

Galvez, M.E., Connolly, J.A.D., Manning, C.E., 2016. Implications for metal and volatile cycles from the pH of subduction zone fluids. Nature 539, 420–424. https://doi.org/10.1038/nature20103.

Galvez, M.E., Manning, C.E., Connolly, J.A.D., Rumble, D., 2015. The solubility of rocks in metamorphic fluids: a model for rock-dominated conditions to upper mantle pressure and temperature. Earth Planet. Sci. Lett. 430, 486–498. https://doi.org/10.1016/j.epsl.2015.06.019.

Gorman, P.J., Kerrick, D.M., Connolly, J.A.D., 2006. Modeling open system metamorphic decarbonation of subducting slabs. Geochem. Geophys. Geosyst. 7.

Green, E., Holland, T., Powell, R., 2007. An order-disorder model for omphacitic pyroxenes in the system jadeite–diopside–hedenbergite–acmite, with applications to eclogitic rocks. Am. Mineral. 92, 1181–1189. https://doi.org/10.2138/Am.2007.2401.

Green, E.C.R., White, R.W., Diener, J.F.A., Powell, R., Holland, T.J.B., Palin, R.M., 2016. Activity-composition relations for the calculation of partial melting equilibria in metabasic rocks. J. Metamorph. Geol. 34, 845–869. https://doi.org/10.1111/jmg.12211.

Harvie, C.E., Greenberg, J.P., Weare, J.H., 1987. A chemical-equilibrium algorithm for highly nonideal multiphase systems – free-energy minimization. Geochim. Cosmochim. Acta 51, 1045–1057. https://doi.org/10.1016/0016-7037(87)90199-2.

Holland, T.J.B., Powell, R., 1998. An internally consistent thermodynamic data set for phases of petrological interest. J. Metamorph. Geol. 16, 309–343.

Kagoshima, T., Sano, Y., Takahata, N., Maruoka, T., Fischer, T.P., Hattori, K., 2015. Sulphur geodynamic cycle. Sci. Rep. 5. https://doi.org/10.1038/srep08330.

Karpov, I.K., Chudnenko, K.V., Kulik, D.A., Avchenko, O.V., Bychinskii, V.A., 2001. Minimization of gibbs free energy in geochemical systems by convex programming. Geochem. Int. 39, 1108–1119.

Kelemen, P.B., Manning, C.E., 2015. Reevaluating carbon fluxes in subduction zones, what goes down, mostly comes up. Proc. Natl. Acad. Sci. USA 112, E3997–E4006. https://doi.org/10.1073/pnas.1507889112.

Kerrick, D.M., Connolly, J.A.D., 2001a. Metamorphic devolatilization of subducted marine sediments and the transport of volatiles into the Earth's mantle. Nature 411, 293–296.

Kerrick, D.M., Connolly, J.A.D., 2001b. Metamorphic devolatilization of subducted oceanic metabasalts: implications for seismicity, arc magmatism and volatile recycling. Earth Planet. Sci. Lett. 189, 19–29.

Lang, S.Q., Fruh-Green, G.L., Bernasconi, S.M., Brazelton, W.J., Schrenk, M.O., McGonigle, J.M., 2018. Deeply-sourced formate fuels sulfate reducers but not methanogens at Lost City hydrothermal field. Sci. Rep. 8. https://doi.org/10.1038/s41598-017-19002-5.

Leal, A.M.M., Kulik, D.A., Smith, W.R., Saar, M.O., 2017. An overview of computational methods for chemical equilibrium and kinetic calculations for geochemical and reactive transport modeling. Pure Appl. Chem. 89, 597–643. https://doi.org/10.1515/pac-2016-1107.

Manning, C.E., 2007. Solubility of corundum plus kyanite in H_2O at 700 degrees C and 10 kbar: evidence for Al–Si complexing at high pressure and temperature. Geofluids 7, 258–269. https://doi.org/10.1111/j.1468-8123.2007.00179.x.

Manning, C.E., Antignano, A., Lin, H.A., 2010. Premelting polymerization of crustal and mantle fluids, as indicated by the solubility of albite plus paragonite plus quartz in H_2O at 1 GPa and 350–620 degrees C. Earth Planet. Sci. Lett. 292, 325–336. https://doi.org/10.1016/j.epsl.2010.01.044.

Manning, C.E., Shock, E.L., Sverjensky, D.A., 2013. The chemistry of carbon in aqueous fluids at crustal and upper-mantle conditions: experimental and theoretical constraints. In: Hazen, R.M., Jones, A.P., Baross, J.A. (Eds.), Carbon in Earth, pp. 109–148.

Mason, E., Edmonds, M., Turchyn, A.V., 2017. Remobilization of crustal carbon may dominate volcanic arc emissions. Science 357. https://doi.org/10.1126/science.aan5049.

Penniston-Dorland, S.C., Kohn, M.J., Manning, C.E., 2015. The global range of subduction zone thermal structures from exhumed blueschists and eclogites: rocks are hotter than models. Earth Planet. Sci. Lett. 428, 243–254. https://doi.org/10.1016/j.epsl.2015.07.031.

Plank, T., Langmuir, C.H., 1998. The chemical composition of subducting sediment and its consequences for the crust and mantle. Chem. Geol. 145, 325–394.

Pokrovski, G.S., Dubrovinsky, L.S., 2011. The S-3(-) ion is stable in geological fluids at elevated temperatures and pressures. Science 331, 1052–1054. https://doi.org/10.1126/science.1199911.

Poli, S., 2015. Carbon mobilized at shallow depths in subduction zones by carbonatitic liquids. Nat. Geosci. 8, 633. https://doi.org/10.1038/ngeo2464.

Prausnitz, J.M., 1969. Molecular Thermodynamics of Fluid-Phase Equilibria. Prentice-Hall, Englewood Cliffs, NJ.

Rupke, L.H., Morgan, J.P., Hort, M., Connolly, J.A.D., 2004. Serpentine and the subduction zone water cycle. Earth Planet. Sci. Lett. 223, 17–34.

Shock, E.L., Oelkers, E.H., Johnson, J.W., Sverjensky, D.A., Helgeson, H.C., 1992. Calculation of the thermodynamic properties of aqueous species at high-pressures and temperatures – effective electrostatic radii, dissociation-constants and standard partial molal properties to 1000 C and 5 kbar. J. Chem. Soc. Faraday Trans. 88, 803–826. https://doi.org/10.1039/ft9928800803.

Skora, S., Blundy, J.D., Brooker, R.A., Green, E.C.R., de Hoog, J.C.M., Connolly, J.A.D., 2015. Hydrous phase relations and trace element partitioning behaviour in calcareous sediments at subduction-zone conditions. J. Petrol. 56, 953–980. https://doi.org/10.1093/petrology/egv024.

Staudigel, H., Hart, S., Schmincke, H., Smith, B., 1989. Cretaceous ocean crust at DSDP sites 417–418: carbon uptake from weathering versus loss by magmatic outgassing. Geochim. Cosmochim. Acta 53, 3091–3094.

Sverjensky, D.A., Harrison, B., Azzolini, D., 2014. Water in the deep Earth: the dielectric constant and the solubilities of quartz and corundum to 60 kb and 1200 degrees C. Geochim. Cosmochim. Acta 129, 125–145. https://doi.org/10.1016/j.gca.2013.12.019.

Sverjensky, D.A., Huang, F., 2015. Diamond formation due to a pH drop during fluid–rock interactions. Nat. Commun. 6. https://doi.org/10.1038/ncomms9702.

Syracuse, E.M., van Keken, P.E., Abers, G.A., 2010. The global range of subduction zone thermal models. Phys. Earth Planet. Inter. 183, 73–90. https://doi.org/10.1016/j.pepi.2010.02.004.

Tsay, A., Zajacz, Z., Ulmer, P., Sanchez-Valle, C., 2017. Mobility of major and trace elements in the eclogite–fluid system and element fluxes upon slab dehydration. Geochim. Cosmochim. Acta 198, 70–91. https://doi.org/10.1016/j.gca.2016.10.038.

Tumiati, S., Tiraboschi, C., Sverjensky, D.A., Pettke, T., Recchia, S., Ulmer, P., Miozzi, F., Poli, S., 2017. Silicate dissolution boosts the CO_2 concentrations in subduction fluids. Nat. Commun. 8. https://doi.org/10.1038/s41467-017-00562-z.

Wolery, T.J., 1992. A Software Package for Geochemical Modeling of Aqueous Systems: Package Overview and Installation Guide. Lawrence Livermore National Laboratory, Livermore, CA.